[177]Lu-Labeled Albumin-Binder–Conjugated PSMA-Targeting Agents with Extremely High Tumor Uptake and Enhanced Tumor-to-Kidney Absorbed Dose Ratio

Hsiou-Ting Kuo[1], Kuo-Shyan Lin[1–3], Zhengxing Zhang[1], Carlos F. Uribe[2], Helen Merkens[1], Chengcheng Zhang[1], and François Bénard[1–3]

[1]Department of Molecular Oncology, BC Cancer, Vancouver, British Columbia, Canada; [2]Department of Functional Imaging, BC Cancer, Vancouver, British Columbia, Canada; and [3]Department of Radiology, University of British Columbia, Vancouver, British Columbia, Canada

The use of an albumin binder has been shown to improve tumor uptake of prostate-specific membrane antigen (PSMA)–targeting radiotherapeutic agents. The aim of this study was to develop improved radiotherapeutic agents that combine an optimized affinity-modifying group and optimized albumin binders to maximize the tumor-to-kidney absorbed dose ratio. **Methods:** ^{68}Ga-labeled DOTA-conjugated lysine-ureido-glutamate–based PSMA-targeting agents bearing various affinity-modifying groups or albumin binders were synthesized and evaluated by PET/CT imaging and biodistribution studies in LNCaP tumor–bearing mice. The optimized affinity-modifying group and albumin binders were combined, and the resulting derivatives were radiolabeled with ^{177}Lu and evaluated by SPECT/CT imaging and biodistribution studies in LNCaP tumor–bearing mice. Radiation dosimetry was calculated using the OLINDA/EXM software. **Results:** Affinity-modifying group optimization revealed that ^{68}Ga-HTK03041 bearing a tranexamic acid-9-anthrylalanine affinity-modifying group had the highest tumor uptake (23.1 ± 6.11 percentage injected dose [%ID]/g at 1 h after injection). Albumin binder optimization showed that ^{68}Ga-HTK03055 and ^{68}Ga-HTK03086 bearing the N-(4-(p-chlorophenyl)butanoyl)-Gly and N-(4-(p-methoxyphenyl)butanoyl)-Gly motifs, respectively, had relatively faster tumor accumulation (~30 %ID/g at 3 h after injection) and lower average kidney uptake (<55 %ID/g at both 1 and 3 h after injection). Combining the tranexamic acid-9-anthrylalanine affinity-modifying group with N-(4-(p-chlorophenyl)butanoyl)-Gly and N-(4-(p-methoxyphenyl)butanoyl)-Gly albumin-binding motifs generated HTK03121 and HTK03123, respectively. ^{177}Lu-HTK03121 and ^{177}Lu-HTK03123 had extremely high peak uptake (104 ± 20.3 and 70.8 ± 23.7 %ID/g, respectively) in LNCaP tumor xenografts, and this peak was sustained up to 120 h after injection. Dosimetry calculation showed that compared with ^{177}Lu-PSMA-617, ^{177}Lu-HTK03121 and ^{177}Lu-HTK03123 delivered 18.7- and 12.7-fold higher absorbed dose to tumor but only 6.4- and 6.3-fold higher absorbed dose to kidneys, leading to 2.9- and 2.0-fold improvement in the tumor-to-kidney absorbed dose ratios. **Conclusion:** With greatly enhanced tumor uptake and tumor-to-kidney absorbed dose ratio, ^{177}Lu-HTK03121 and ^{177}Lu-HTK03123 have the potential to improve treatment efficacy using significantly lower quantities of ^{177}Lu and are promising candidates for clinical translation to treat metastatic castration-resistant prostate cancer.

Radioligands targeting the prostate-specific membrane antigen (PSMA), a transmembrane enzyme that catalyzes the hydrolysis of N-acetyl-aspartylglutamate, have been actively developed in the past few years to treat metastatic castration-resistant prostate cancer (1,2). Leading the field is ^{177}Lu-PSMA-617, currently under investigation in a phase III clinical trial (3). A recent German retrospective multicenter study (4) showed that most patients (60%, 59/99) had a prostate-specific antigen response after ^{177}Lu-PSMA-617 therapy, and 45% had more than a 50% prostate-specific antigen reduction. An Australian prospective study conducted by Hofman et al. showed comparable response rates, with significant symptomatic improvement in patients with advanced metastatic prostate cancer (5). Despite these successes, many patients have an insufficient response to radioligand therapy and experience disease progression during or after treatment.

One strategy to enhance treatment efficacy is to improve radioligand delivery to maximize the radiation dose to tumor cells. This has been achieved by conjugating an albumin-binding motif to PSMA-targeting radioligands to extend the blood residence time and maximize tumor uptake (6–12). Despite enhanced tumor uptake, greatly increased kidney uptake was also commonly observed, leading to a reduced tumor-to-kidney absorbed dose ratio. Previously, we reported an 8.3-fold increase in tumor-absorbed dose after conjugating an N-(4-(p-iodophenyl)butanoyl)-Glu albumin-binding motif to the pharmacophore of ^{177}Lu-PSMA-617. However, the resulting ^{177}Lu-HTK01169 (Fig. 1) also delivered a 17.1-fold higher absorbed dose to kidneys, leading to an approximately 50% reduction in the tumor-to-kidney absorbed dose ratio (8).

The improvement in tumor-to-kidney absorbed dose ratio for albumin-binder–conjugated PSMA-targeting radiotherapeutic agents can be achieved by increasing tumor uptake or decreasing kidney uptake. The lipophilic affinity-modifying group of PSMA-617 (tranexamic acid-2-naphthylalanine) was selected after evaluating
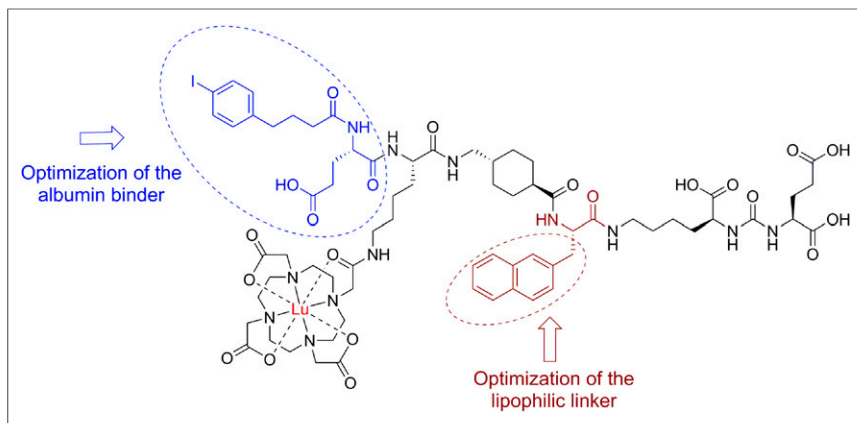
FIGURE 1. Strategies for structural optimization of Lu-HTK01169 to further improve tumor uptake and tumor-to-kidney absorbed dose ratio.

18 candidates (*13*). Our recent attempt to replace the 2-naphthylalanine in PSMA-617 did not result in higher tumor uptake (*14*). However, further optimization might lead to novel derivatives with higher tumor uptake.

Umbricht et al. reported that the use of a weaker albumin binder with faster blood clearance and lower background uptake (including kidneys) achieved comparable tumor uptake, leading to improvement in tumor-to-background (including kidneys) absorbed dose ratios (*10*). These data suggest that optimization of the albumin-binding motif could be an effective strategy to reduce kidney-absorbed dose without sacrificing the tumor-absorbed dose.

We aimed to improve the tumor-to-kidney absorbed dose ratio of ^{177}Lu-HTK01169 by optimizing both the lipophilic affinity-modifying group and the albumin-binding motif (Fig. 1). To optimize the lipophilic affinity-modifying group (Fig. 2), we replaced the 2-naphthylalanine in PSMA-617 with 2-aminooctanoic acid (HTK03026), 2-anthrylalanine (HTK03027), 1-pyrenylalanine (HTK03029), or 9-anthrylalanine (HTK03041). To optimize the albumin binder, we replaced the *N*-(4-(*p*-iodophenyl)butanoyl)-Glu albumin-binding motif in HTK01169 with a *p*-substituted *N*-(4-(phenyl)butanoyl)-Gly, and we varied the substituents from I, Br, Cl, F, CH₃,
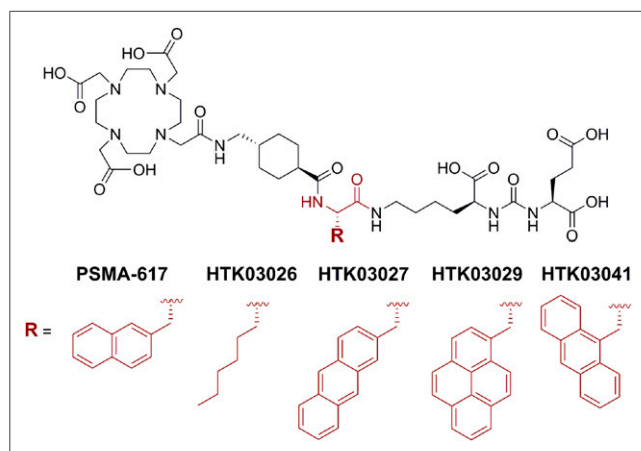
FIGURE 2. Chemical structures of PSMA-617 and derivatives with 2-naphthylalanine in PSMA-617 substituted with 2-aminooctanoic acid (HTK03026), 2-anthrylalanine (HTK03027), 1-pyrenylalanine (HTK03029), or 9-anthrylalanine (HTK03041).

OCH₃, NO₂, and NH₂. On the basis of the tumor or kidney uptake of their ^{68}Ga-labeled analogs, we selected an optimized lipophilic affinity-modifying group and 2 albumin-binding motifs to generate our top 2 candidates, HTK03121 and HTK03123. Subsequently, we evaluated both ^{177}Lu-labeled HTK03121 and HTK03123 by SPECT/CT imaging and biodistribution studies in mice bearing PSMA-expressing LNCaP tumor xenografts, and we evaluated their tumor-to-kidney absorbed dose ratios by radiation dosimetry calculation.

MATERIALS AND METHODS

Detailed procedures and results for the synthesis and purification of DOTA-conjugated peptidomimetics, their nonradioactive Ga- and Lu-complexed standards, and [68]Ga- and ^{177}Lu-labeled analogs are provided in the supplemental materials (available at http://jnm.snmjournals.org) (*13,15–25*).

All chemicals and solvents were obtained from commercial sources and used without further purification. PSMA-targeting peptides were synthesized using the solid-phase approach on an AAPPTec Endeavor 90 peptide synthesizer. Purification and quality control of nonradioactive and radiolabeled peptides were performed on Agilent high-performance liquid chromatography (HPLC) systems equipped with a model 1200 quaternary pump, a model 1200 ultraviolet absorbance detector (set at 220 nm), and a Bioscan NaI scintillation detector. The operation of Agilent HPLC systems was controlled using the Agilent ChemStation software. The HPLC columns included a semipreparative column (Luna C18, 5 μm, 250 × 10 mm) and an analytic column (Luna C18, 5 μm, 250 × 4.6 mm) purchased from Phenomenex. The collected HPLC eluates containing the desired peptide were lyophilized using a Labconco FreeZone 4.5 Plus freeze-drier. Mass analyses were performed using an AB Sciex 4000 QTRAP mass spectrometer system with an electrospray ion source. C18 Sep-Pak cartridges (1 cm³, 50 mg) were obtained from Waters. [68]Ga was eluted from an iThemba Labs generator and purified according to previously published procedures using a *N,N,N′,N′*-tetra-*n*-octyldiglycolamide column from Eichrom Technologies LLC (*15*). [177]LuCl₃ solution was ordered from ITG Isotope Technologies Garching Gmbh. The radioactivity of [68]Ga- and ^{177}Lu-labeled peptides was measured using a Capintec CRC-25R/W dose calibrator, and the radioactivity of mouse tissues collected from biodistribution studies were counted using a Perkin Elmer Wizard² 2480 automatic γ-counter.

Radiation Dosimetry Calculation

Internal dosimetry was estimated using the OLINDA software, version 2.0 (*20*). These estimates were performed for mice using the 25-g mouse whole-body phantom (*21*), for humans using the nonuniform rational-basis spline model for the adult male (*22*), and for tumors using the previously reported unit density sphere model (*23*). All the phantoms and the sphere model are available in OLINDA and require input of the total number of decays normalized by injected activity in units of MBq × h/MBq for each source organ or tumor.

The biodistribution data (available in Supplemental Tables 1 and 2) were used to determine the kinetic input values required by OLINDA. First, each value was decayed to its corresponding time point (the values in the table are shown at injection time). Then, the different time-points of the uptake data (percentage injected dose [%ID]/g) for each organ were fitted to both monoexponential ($\frac{\%ID}{g} = ae^{-bt}$) and

biexponential ($\frac{\%ID}{g} = ae^{-bt} + ce^{-dt}$) functions using in-house software developed in Python. The selection of best fit was based on maximizing the coefficient of determination (R^2) of the fit and minimizing the residuals. The areas under the curves were analytically calculated on the basis of the parameters obtained from the best fit of each organ, and this calculation provided the kinetic input values required by OLINDA.

In the mouse case, the adrenals, blood, fat, muscle, and seminal vesicles are not modeled in the phantom. These organs were grouped and included in what OLINDA calls the remainder of the body.

The mouse biodistribution data were extrapolated to humans using a method proposed by Kirschner et al (24)::

$$\left(\frac{\%ID}{m_{organ}}\right)_{human} = \left(\frac{\%ID}{m_{organ}}\right)_{mouse} \left[\frac{M_{mouse}}{M_{human}} \times (m_{organ})_{human}\right],$$

where m_{organ} is the mass of the organ and M represents the total-body mass. Masses for the organs and total body weight were taken from the simulated masses of the phantoms in OLINDA. Because the biodistribution data do not differentiate between left colon, right colon, and rectum, which are present in the OLINDA human phantom, it was assumed that in the biodistribution, these 3 regions of the intestine have the same %ID/g as the large intestine. The %ID/g for the blood was assumed to be that for the heart contents of the phantom. This value was also used to calculate the bone marrow uptake using a method described by Wessels et al. (25) in which we assumed a hematocrit fraction of 0.40 based on the patient values shown in that study. At the end, red marrow values used the blood measurements scaled by a factor of 0.32. In the human case, because the fat, muscle, and seminal vesicles that are present in the biodistribution data are not modeled in the phantom, the numbers of decays present in these regions were included in the remainder of the body. The data were again fitted as for the mouse case, and the values for the total number of decays, in units of MBq × h/MBq, were inputted into OLINDA.

Lastly, the numbers of decays in the tumors were also calculated on the basis of the biodistribution data of the mice, and the values were inputted into the sphere model available in OLINDA.

Cell Culture

The LNCaP cells obtained from ATCC (via Cedarlane) were cultured in RPMI 1640 medium supplemented with 10% fetal bovine serum, penicillin (100 U/mL), and streptomycin (100 μg/mL) at 37°C in a Panasonic Health Care MCO-19AIC humidified incubator containing 5% CO_2. The cells were confirmed pathogen-free by the IMPACT Rodent Pathogen Test (IDEXX BioAnalytics). Cells grown to 80%–90% confluence were then washed with sterile phosphate-buffered saline (pH 7.4) and collected after trypsinization. The cell concentration was counted in triplicate using a hemocytometer and a manual laboratory counter.

In Vitro Competition Binding Assays

The binding assays were conducted following previously published procedures using LNCaP cells and ^{18}F-DCFPyL as the radioligand (8,14,26). Data analyses of binding affinity (K_i) were performed using the nonlinear regression algorithm of GraphPad Prism 7 software.

Biodistribution and Imaging Studies

Imaging and biodistribution experiments were performed following previously published procedures using male NOD-*scid* IL2Rg[null] mice for the ^{68}Ga-labeled compounds and NOD.Cg-Rag1[tm1Mom] Il2rg[tm1Wjl]/SzJ mice for the ^{177}Lu-labeled compounds (8,14,26). The experiments were conducted according to the guidelines established by the Canadian Council on Animal Care and approved by the Animal Ethics Committee of the University of British Columbia. The mice were briefly sedated by inhalation of 2% isoflurane in oxygen and received a subcutaneous implant of 1×10^7 LNCaP cells behind the left shoulder. The mice were imaged or used in biodistribution studies when the tumor grew to 5–8 mm in diameter over 4–5 wk.

PET/CT imaging experiments were conducted using a Siemens Inveon small-animal PET/CT scanner. Each tumor-bearing mouse was injected with about 6–8 MBq of ^{68}Ga-labeled tracer through a lateral caudal tail vein. After 50 min after injection, a 10-min CT scan was conducted first for localization and attenuation correction after segmentation for reconstructing the PET images; this scan was followed by a 10-min static PET acquisition. For ^{68}Ga-HTK03041, the mouse imaged at 1 h after injection was imaged again at 3 h by repeating the CT scan and then obtaining a 15-min static PET acquisition.

SPECT/CT imaging experiments were conducted using the MILabs U-SPECT-II/CT scanner. Each tumor-bearing mouse was injected with about 37 MBq of ^{177}Lu-labeled compound through a lateral caudal tail vein. The mice were imaged at 1, 4, 24, 72, and 120 h after injection. At each time point, a 5-min CT scan was conducted first for anatomic reference; afterward, two 30-min static emission scans were acquired in list mode.

For biodistribution studies, the mice were injected with the radiotracer (2–4 MBq) as described above. For blocking, the mice were coinjected with nonradioactive DCFPyL (0.5 mg). At predetermined time points, the mice were sedated by isoflurane inhalation and euthanized by CO_2 inhalation. Blood was withdrawn by cardiac puncture, and organs or tissues of interest were collected, weighed, and counted using a Perkin Elmer Wizard² 2480 automatic γ-counter.

Statistical Analysis

Statistical analyses were performed by Student *t* testing using Microsoft Excel software. The unpaired, 2-tailed test was used to compare the PSMA K_i of Ga-PSMA-617 with that of HTK03026, HTK03027, HTK03029, or HTK03041. The difference was considered statistically significant when the P value was less than 0.05.

RESULTS

#### Optimization of the Lipophilic Linker and Affinity-Modifying Group

Replacing the 2-naphthylalanine in Ga-PSMA-617 with 2-aminooctanoic acid, 2-anthrylalanine, 1-pyrenylalanine, or 9-anthrylalanine generated Ga-HTK03026, Ga-HTK03027, Ga-HTK03029, or Ga-HTK03041, respectively (Fig. 2; Supplemental Tables 1–3). Ga-HTK03026, Ga-HTK03027, Ga-HTK03029, and Ga-HTK03041 inhibited the binding of ^{18}F-DCFPyL to LNCaP cells in a dose-dependent manner (Supplemental Fig. 1), and their calculated K_i values were 48.2 ± 16.8, 18.8 ± 8.45, 16.6 ± 3.61, and 0.63 ± 0.06 nM ($n = 3$), respectively. All tracers were excreted predominately via the renal pathway, and ^{68}Ga-HTK03026 had the lowest kidney uptake and the lowest overall background uptake (Fig. 3). All tracers enabled clear visualization of tumors on PET images at 1 h after injection, and the tumor uptake of ^{68}Ga-HTK03041 was highest. The biodistribution data (Supplemental Table 4) were consistent with observations on PET images, with ^{68}Ga-HTK03026 having the lowest uptake in all collected organs or tissues. The tumor uptake of ^{68}Ga-HTK03041 was 23.1 ± 6.11 %ID/g at 1 h after injection and increased to 28.2 ± 9.17 %ID/g at 3 h after injection. Blocking with DCFPyL reduced tumor uptake of ^{68}Ga-HTK03041 by more than 95%, demonstrating that the uptake in tumor was PSMA-mediated.
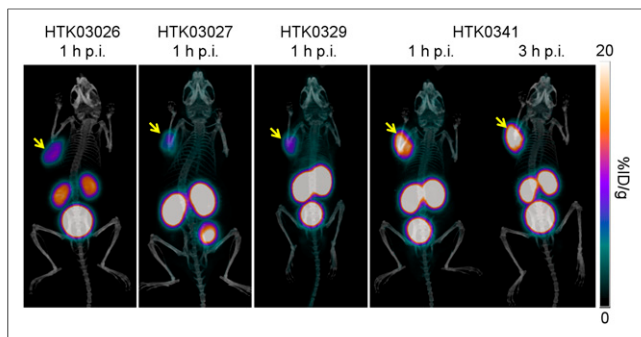
FIGURE 3. Representative PET/CT images of ^{68}Ga-HTK03026, ^{68}Ga-HTK03027, ^{68}Ga-HTK03029, and ^{68}Ga-HTK03041 in mice bearing LNCaP tumor xenografts. p.i. = after injection.

Optimization of the Albumin Binder

PET/CT imaging and biodistribution studies were conducted for ^{68}Ga-labeled HTK01169 derivatives (Fig. 4; Supplemental Tables 5–7) bearing various albumin binders. The derivatives with the albumin binder substituted with I (^{68}Ga-HTK03025), Br (^{68}Ga-HTK03058), Cl (^{68}Ga-HTK03055), and CH$_3$ (^{68}Ga-HTK03090) resulted in a higher retention in the blood pool than did those with OCH$_3$ (^{68}Ga-HTK03086), NO$_2$ (^{68}Ga-HTK03089), F (^{68}Ga-HTK03085), and NH$_2$ (^{68}Ga-HTK03087) substitutions (Supplemental Fig. 2). A lower background level was observed at 3 h after injection for all derivatives, and higher tumor uptake was observed at 3 h after injection for all derivatives except the NH$_2$-substituted ^{68}Ga-HTK03087. On the basis of their biodistribution data (Supplemental Table 8), the average blood retention (%ID/g at 1 and 3 h after injection) of these derivatives generally followed the lipophilicity order (Supplemental Fig. 3) of the substituents (with the exception of the F-substituted ^{68}Ga-HTK03085): I (27.0 ± 5.63, 23.9 ± 1.03) > Br (26.7 ± 3.02, 21.2 ± 2.21) > Cl (22.1 ± 2.04, 17.4 ± 1.15) > CH$_3$ (17.0 ± 1.81, 13.0 ± 0.63) > OCH$_3$ (12.1 ± 0.60, 6.60
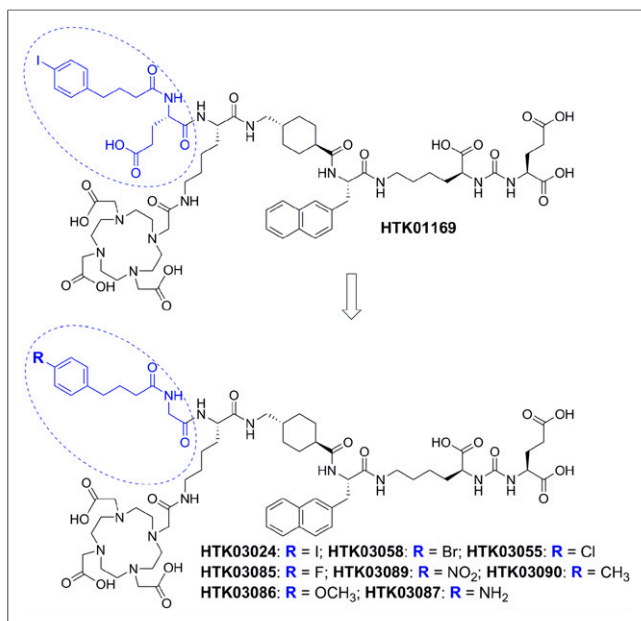
± 0.84) > NO$_2$ (6.69 ± 0.27, 2.52 ± 0.69) > F (5.73 ± 0.93, 2.10 ± 0.48) > NH$_2$ (1.74 ± 0.11, 0.52 ± 0.08). Conversely, the average tumor uptake (%ID/g at 1 h after injection) was generally inversely correlated to the lipophilicity of the substituents: NO$_2$ (21.7 ± 2.48) > NH$_2$ (20.7 ± 3.79) > F (18.8 ± 3.35) > OCH$_3$ (17.8 ± 2.89) > Cl (17.2 ± 1.67) > CH$_3$ (12.9 ± 4.26) > Br (11.2 ± 3.33) > I (7.34 ± 0.10). Among these derivatives, the Cl- and OCH$_3$-substituted albumin binders in ^{68}Ga-HTK03055 and ^{68}Ga-HTK03086, respectively, resulted in moderate blood retention and relatively faster tumor uptake (∼30 %ID/g at 3 h after injection) and lower average kidney uptake (up to ∼55 %ID/g) and were selected for further evaluation.

Top Candidates Combining the Optimized Lipophilic Affinity-Modifying Group and Albumin Binders

The optimized 9-anthrylalanine–containing affinity-modifying group was combined with the selected Cl- and OCH$_3$-substituted albumin binders to generate 2 novel albumin-binder–conjugated derivatives, HTK03121 and HTK03123, respectively (Fig. 5; Supplemental Tables 9–11). Both Lu-HTK03121 and Lu-HTK03123 inhibited the binding of ^{18}F-DCFPyL in a dose-dependent manner (Supplemental Fig. 1), and their calculated K_i values were 1.69 ± 1.22 and 1.76 ± 0.69 ($n = 3$), respectively. SPECT/CT imaging (Fig. 6) and biodistribution studies (Supplemental Tables 12–13) showed that both ^{177}Lu-HTK03121 and ^{177}Lu-HTK03123 were excreted mainly via the renal pathway and achieved extremely high and sustained tumor uptake (104 ± 20.3 and 70.8 ± 23.7 %ID/g, respectively) at 24 h after injection. Compared with ^{177}Lu-HTK03121, ^{177}Lu-HTK03123 had faster clearance from blood, leading to relatively lower uptake in most of the collected organs or tissues, especially at later time points.

The results of dosimetry calculations are provided in Supplemental Tables 14–17. For a 500-mg lesion, the absorbed doses to the tumors were 11,100 and 7,540 mGy/MBq for ^{177}Lu-HTK03121 and ^{177}Lu-HTK03123, respectively, compared with 4,960 and 594 mGy/MBq for the previously reported ^{177}Lu-HTK01169 and ^{177}Lu-PSMA-617, respectively (Fig. 7A), in the same tumor model (8). The kidney doses were 18.1, 17.7, 48.2, and 2.82 mGy/MBq for ^{177}Lu-HTK03121, ^{177}Lu-HTK03123, ^{177}Lu-HTK01169, and ^{177}Lu-PSMA-617, respectively, leading to tumor-to-kidney absorbed dose ratios of 613, 426, 103, and 211, respectively (Fig. 7B). Thus, compared with ^{177}Lu-HTK01169 and ^{177}Lu-PSMA-617, ^{177}Lu-HTK03121 delivered a 2.2- and 18.7-fold higher absorbed dose to tumor and had a 6.0- and 2.9-fold improvement in the tumor-to-kidney absorbed dose ratio. Similarly, compared with ^{177}Lu-HTK01169 and ^{177}Lu-PSMA617, ^{177}Lu-HTK03123
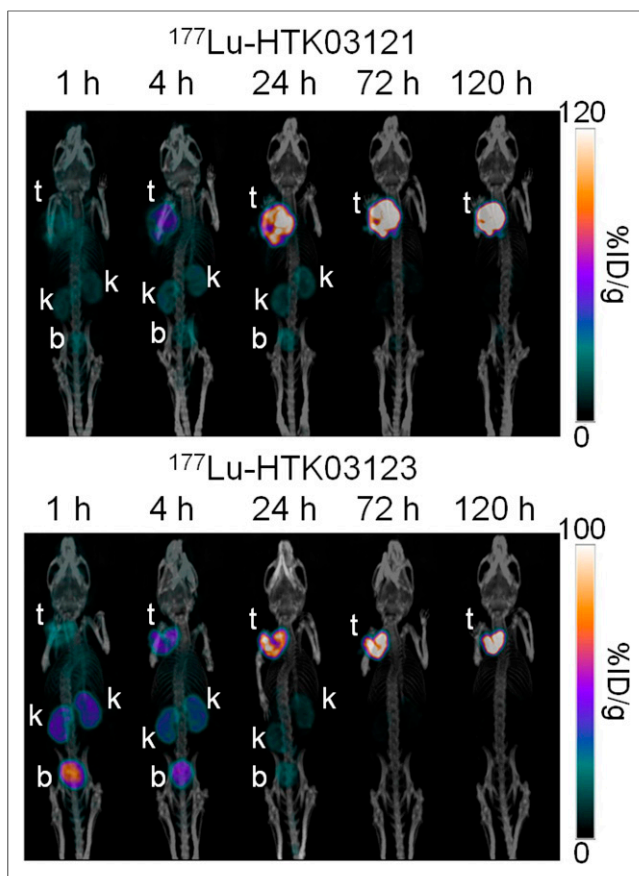

FIGURE 4. Chemical structures of HTK01169 derivatives bearing various albumin-binding motifs.
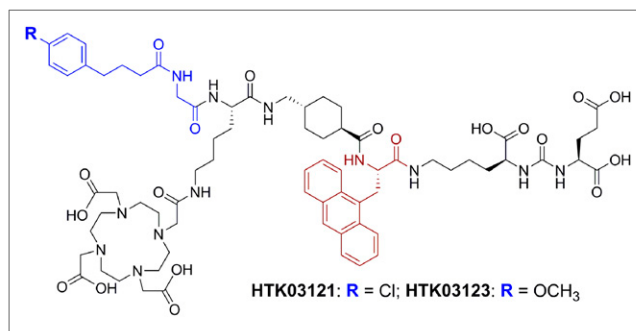

FIGURE 5. Chemical structures of HTK03121 and HTK03123.

FIGURE 6. Maximum-intensity-projection SPECT/CT images of ^{177}Lu-HTK03121 (top) and ^{177}Lu-HTK03123 (bottom) acquired at predetermined time points in mice bearing LNCaP tumor xenografts. b = urinary bladder; k = kidney; t = tumor.

also delivered 1.5- and 12.7-fold higher absorbed dose to tumor and had 4.1- and 2.0-fold improvement in the tumor-to-kidney absorbed dose ratio.

DISCUSSION

We replaced the 2-naphthyl group in 2-naphthylalanine with a flexible n-pentyl group (HTK03026) or a larger fused aromatic ring (2-anthryl in HTK03027, 1-pyrenyl in HTK03029, or
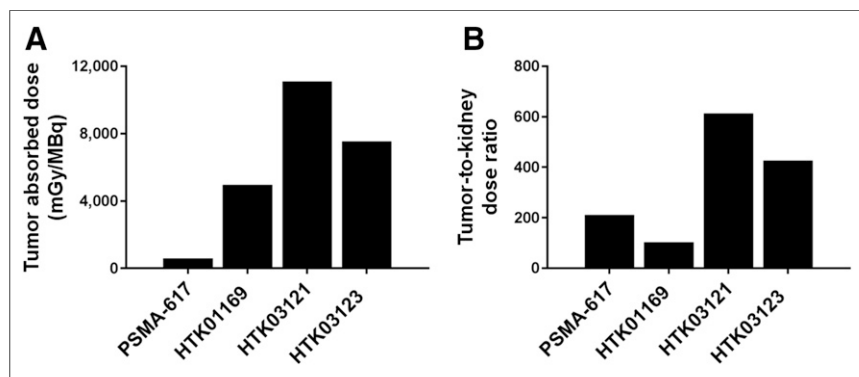
FIGURE 7. Comparison of tumor-absorbed dose (A) and tumor-to-kidney absorbed dose ratio (B) between ^{177}Lu-labeled PSMA-617, HTK01169, HTK03121, and HTK03123.

9-anthryl in HTK03041). Although Ga-HTK03026, Ga-HTK03027, and Ga-HTK03029 had a lower PSMA binding affinity (K_i = 48.2 ± 16.8, 18.8 ± 8.45, and 16.6 ± 3.61 nM vs. 1.23 ± 0.08 nM of Ga-PSMA-617, $P < 0.05$) (14), replacing the 2-naphthyl group with a 9-anthryl group significantly enhanced the binding affinity (K_i for HTK03041: 0.63 ± 0.06 nM, $P < 0.001$). The observed enhancement in PSMA binding affinity was consistent with the improved tumor uptake of ^{68}Ga-HTK03041 (23.1 ± 6.11 %ID/g at 1 h after injection), compared with ^{68}Ga-HTK03026 (12.5 ± 2.90 %ID/g), ^{68}Ga-HTK03027 (13.3 ± 5.44 %ID/g), ^{68}Ga-HTK03029 (13.9 ± 6.58 %ID/g), and the previously reported ^{68}Ga-PSMA-617 (16.7 ± 2.30 %ID/g) using the same LNCaP tumor model (14). Therefore, the tranexamic acid-9-anthrylalanine was selected as our optimized linker and affinity-modifying group.

We replaced the N-(4-(p-iodophenyl)butanoyl)-Glu group in HTK01169 with a p-substituted (4-(phenyl)butanoyl)-Gly group (Fig. 4). The free carboxylate at the Glu side chain of the N-(4-(p-iodophenyl)butanoyl)-Glu group was designed to mimic the α-carboxylate group of the albumin-binding N^2-acetyl-N^6-(4-(p-iodophenyl)butanoyl)-D-Lys group originally reported by Dumelin et al. (27). However, Benešová et al. (9) showed that the free carboxylate group was not required for binding to albumin, and in fact, albumin-binding motifs containing one or more free carboxylate groups led to derivatives with a higher kidney uptake. Therefore, we replaced the Glu in the N-(4-(p-iodophenyl)butanoyl)-Glu group with a Gly to remove the free carboxylate group. In addition, we replaced the iodo group with various substituents from a highly lipophilic bromo group to a very hydrophilic amino group (Fig. 4).

As shown in Supplemental Figures 2–3 and Supplemental Table 8, the blood retention of these ^{68}Ga-labeled derivatives followed the lipophilicity order of the substituents (with the exception of the F-substituted ^{68}Ga-HTK03085), ranging from very high (27.0 ± 5.63 %ID/g at 1 h after injection for the I-substituted ^{68}Ga-HTK03025) to low (1.74 ± 0.11 %ID/g at 1 h after injection for the NH_2-substituted ^{68}Ga-HTK03087). These data are of great importance because they provide a library of albumin-binding motifs with various clearance rates from the blood pool. The average tumor uptake of these ^{68}Ga-labeled derivatives was generally inversely correlated to the lipophilicity of the substituents, because derivatives with tighter binding to albumin would have fewer opportunities to bind to PSMA at early time points.

The combination of the optimized affinity-modifying group and albumin binders generated HTK03121 and HTK03123. The PSMA binding affinity of Lu-HTK03121 (2.40 ± 0.10 nM) and Lu-HTK03123 (1.76 ± 0.69 nM) were close to that of Ga-HTK03041 (0.63 ± 0.06 nM). This finding suggests that adding an albumin-binding motif to the core structure of HTK03041 and replacing the Ga-DOTA complex with a Lu-DOTA complex had a minor impact on the overall PSMA binding affinity. The blood retention values of the Cl-substituted ^{68}Ga-HTK03055 at 1 h (22.1 ± 2.04 %ID/g) and 3 h after injection (17.4 ± 1.15 %ID/g) were comparable to those of the Cl-substituted ^{177}Lu-HTK03121 at 1 h (22.6 ± 5.35 %ID/g) and 4 h after injection (15.3 ± 2.07 %ID/g), respectively. Similarly, the blood retention values

of the OCH$_3$-substituted ^{68}Ga-HTK03086 at 1 h (12.1 ± 0.60 %ID/g) and 3 h after injection (6.60 ± 0.84 %ID/g) were comparable to those of the OCH$_3$-substituted ^{177}Lu-HTK03123 at 1 h (14.1 ± 1.01 %ID/g) and 4 h after injection (7.30 ± 1.39 %ID/g), respectively. These data indicate that the blood retention of these radioligands was driven primarily by the albumin-binding motif, and replacing the 2-naphthylalanine and ^{68}Ga-DOTA complex in ^{68}Ga-HTK03055 and ^{68}Ga-HTK03086 with a 9-anthrylalanine and ^{177}Lu-DOTA complex, respectively, had little effect on their overall blood retention.

Similar to the biodistribution data of ^{68}Ga-HTK03055 and ^{68}Ga-HTK03086, ^{177}Lu-HTK03121 and ^{177}Lu-HTK03123 also showed relatively lower uptake in the kidneys. Unlike ^{177}Lu-HTK01169, which had high and prolonged kidney uptake (125 %ID/g at 24 h after injection) (8), the kidney uptake of both ^{177}Lu-HTK03121 and ^{177}Lu-HTK03123 peaked at 4 h after injection and cleared at a faster pace. Dosimetry calculations showed that compared with ^{177}Lu-HTK01169, the kidney-absorbed dose was about 62% lower with ^{177}Lu-HTK03121 and ^{177}Lu-HTK03123.

Compared with ^{177}Lu-HTK01169, ^{177}Lu-HTK03121 and ^{177}Lu-HTK03123 showed, respectively, 86% and 23% increases in peak tumor uptake and 123% and 52% increases in tumor-absorbed dose. High tumor uptake values reaching 104 %ID/g were achieved by combining an improved affinity-modifying group with a moderate albumin binder, using an endogenously expressing LNCaP tumor model. These increases in tumor-absorbed dose and the reductions in kidney-absorbed dose by ^{177}Lu-HTK03121 and ^{177}Lu-HTK03123 led to a 6.0- and 4.1-fold improvement, respectively, in tumor-to-kidney absorbed dose ratio when compared with that of ^{177}Lu-HTK01169. Even compared with the clinical candidate ^{177}Lu-PSMA-617, ^{177}Lu-HTK03121 and ^{177}Lu-HTK03123 still showed a 2.9- and 2.0-fold improvement in the tumor-to-kidney absorbed dose ratio, respectively, mainly attributed to their extremely high tumor-absorbed dose.

Other strategies, including the use of radioligands with a lower molar activity (28,29) or blocking with a PSMA inhibitor (such as 2-PMPA) (30–32), have been explored to reduce the kidney uptake of PSMA-targeting radioligands. However, such strategies generally lead to reduction of tumor uptake as well and are not suitable for clinical translation. Previously, we reported the administration of monosodium glutamate, a well-known food additive, to reduce kidney and salivary gland uptake without affecting uptake of ^{68}Ga-PSMA-11 in LNCaP tumor xenografts (33). However, a recent clinical study using ^{18}F-DCFPyL demonstrated that monosodium glutamate (34) treatment reduced uptake not only in kidneys and salivary glands but also in malignant lesions, limiting the use of monosodium glutamate as a renal protection agent for radioligand therapy.

With ^{177}Lu-PSMA-617, the administered activity is constrained in part by theoretic radiation exposure limits to the kidneys and salivary glands. Because of the low uptake of PSMA radiotracers in its salivary glands, the mouse is not a suitable animal model to assess salivary gland dosimetry of PSMA-targeting radioligands (9,35). Therefore, our efforts in this report focused on enhancing the tumor-to-kidney absorbed dose ratio of ^{177}Lu-labeled albumin-binder–conjugated PSMA-targeting agents. Since bone marrow radiation exposure is driven primarily by secondary exposure from bone metastases (36), the use of an albumin binder is not likely to lower the risk of hematologic toxicity.

With significantly improved radiation delivery to prostate tumors, and an enhanced tumor-to-kidney absorbed dose ratio,

^{177}Lu-HTK03121 and ^{177}Lu-HTK03123 are potential candidates for clinical translation to treat metastatic castration-resistant prostate cancer. These compounds offer potential for enhanced treatment efficacy using a fraction of the required injected activity of ^{177}Lu-PSMA-617. With a finite supply and growing demand for ^{177}Lu, this enhanced efficacy can reduce manufacturing costs and improve patient access to prostate cancer radioligand therapy. In addition, handling lower amounts of ^{177}Lu can lower exposure of the hospital staff and the public to radiation and reduce shielding requirements for treatment facilities. This benefit can improve treatment workflow, as patients can be discharged shortly after injection without the need to wait (typically 3–4 h in North America) for the injected radioactivity to clear or decay to acceptable levels. A more optimal use of administered ^{177}Lu also reduces unnecessary radioactive waste in sewer systems after patients are released.

Our study had some limitations. First, we did not measure the PSMA binding affinities of Ga-complexed albumin-binder–conjugated ligands. These data would be helpful to tease out the effect of the lipophilicity of albumin-binding motifs on their overall binding to PSMA. Second, we did not measure the albumin binding affinities of Ga-complexed albumin-binder–conjugated ligands. These data would be helpful to determine the range of albumin binding affinity for radioligands with suitable blood residence times. Third, we did not conduct the radiotherapy study using ^{177}Lu-HTK03121 and ^{177}Lu-HTK03123. Therefore, further studies are needed to verify if their enhanced tumor-absorbed doses and tumor-to-kidney dose ratios obtained from radiation dosimetry calculations can be directly translated to improved treatment efficacy and reduced renal toxicity.

CONCLUSION

We optimized the selection of the albumin binder and lipophilic affinity-modifying group for the design of ^{177}Lu-labeled PSMA-targeting radiotherapeutic agents to enhance the tumor-to-kidney absorbed dose ratio. The combination of the optimized affinity-modifying group and the optimized albumin binders generated ^{177}Lu-HTK03121 and ^{177}Lu-HTK03123, which showed not only greatly enhanced tumor-absorbed doses (>12-fold) but also higher tumor-to-kidney absorbed dose ratios (≥2.0-fold) than those of ^{177}Lu-PSMA-617. Both ^{177}Lu-HTK03121 and ^{177}Lu-HTK03123 are promising for clinical translation to treat metastatic castration-resistant prostate cancer, as they are expected to achieve better treatment efficacy with only a fraction of the dose of ^{177}Lu-PSMA-617 and cause less kidney damage. The evaluated albumin-binding motifs provide a library of compounds that confer various blood retention times for their conjugates. Depending on the targets and targeting vectors, this library of compounds offers a great selection of albumin-binding motifs to further enhance blood retention and tumor uptake of targeted radiopharmaceuticals.

DISCLOSURE

KEY POINTS

QUESTION: Can the tumor-to-kidney absorbed dose ratios of ^{177}Lu-labeled albumin-binder–conjugated PSMA-targeting radioligands be improved to be comparable to or even better than that of ^{177}Lu-PSMA-617?

PERTINENT FINDINGS: With an optimized lipophilic affinity-modifying group and albumin binder, both ^{177}Lu-HTK03121 and ^{177}Lu-HTK03123 showed not only a greatly enhanced absorbed dose to tumor, compared with ^{177}Lu-PSMA-617, but also improved tumor-to-kidney absorbed dose ratios.

IMPLICATIONS FOR PATIENT CARE: The use of ^{177}Lu-HTK03121 or ^{177}Lu-HTK03123 can achieve the same treatment efficacy with only a fraction of the dose of ^{177}Lu-PSMA-617 and cause less renal damage.

REFERENCES

1. Virgolini I, Decristoforo C, Haug A, Fanti S, Uprimny C. Current status of theranostics in prostate cancer. *Eur J Nucl Med Mol Imaging.* 2018;45: 471–495.
2. Rahbar K, Afshar-Oromieh A, Jadvar H, Ahmadzadehfar H. PSMA theranostics: current status and future directions. *Mol Imaging.* 2018;17:1536012118776068.
3. Study of 177Lu-PSMA-617 In Metastatic Castrate-Resistant Prostate Cancer (VISION). https://clinicaltrials.gov/ct2/show/NCT03511664. Published April 30. 2018. Updated September 7, 2020. Accessed November 12, 2020.
4. Rahbar K, Ahmadzadehfar H, Kratochwil C, et al. German multicenter study investigating ^{177}Lu-PSMA-617 radioligand therapy in advanced prostate cancer patients. *J Nucl Med.* 2017;58:85–90.
5. Hofman MS, Violet J, Hicks RJ, et al. [^{177}Lu]-PSMA-617 radionuclide treatment in patients with metastatic castration-resistant prostate cancer (LuPSMA trial): a single-centre, single-arm, phase 2 study. *Lancet Oncol.* 2018;19: 825–833.
6. Wang Z, Tian R, Niu G, et al. Single low-dose injection of Evans blue modified PSMA-617 radioligand therapy eliminates prostate-specific membrane antigen positive tumors. *Bioconjug Chem.* 2018;29:3213–3221.
7. Deberle LM, Benešová M, Umbricht CA, et al. Development of a new class of PSMA radioligands comprising ibuprofen as an albumin-binding entity. *Theranostics.* 2020;10:1678–1693.
8. Kuo HT, Merkens H, Zhang Z, et al. Enhancing treatment efficacy of ^{177}Lu-PSMA-617 with the conjugation of an albumin-binding motif: preclinical dosimetry and endoradiotherapy studies. *Mol Pharm.* 2018;15:5183–5191.
9. Benešová M, Umbricht CA, Schibli R, Muller C. Albumin-binding PSMA ligands: optimization of the tissue distribution profile. *Mol Pharm.* 2018;15: 934–946.
10. Umbricht CA, Benešová M, Schibli R, Muller C. Preclinical development of novel PSMA-targeting radioligands: modulation of albumin-binding properties to improve prostate cancer therapy. *Mol Pharm.* 2018;15:2297–2306.
11. Choy CJ, Ling X, Geruntho JJ, et al. ^{177}Lu-labeled phosphoramidate-based PSMA inhibitors: the effect of an albumin binder on biodistribution and therapeutic efficacy in prostate tumor-bearing mice. *Theranostics.* 2017;7:1928–1939.
12. Kelly J, Amor-Coarasa A, Ponnala S, et al. Trifunctional PSMA-targeting constructs for prostate cancer with unprecedented localization to LNCaP tumors. *Eur J Nucl Med Mol Imaging.* 2018;45:1841–1851.
13. Benešová M, Bauder-Wust U, Schafer M, et al. Linker modification strategies to control the prostate-specific membrane antigen (PSMA)-targeting and pharmacokinetic properties of DOTA-conjugated PSMA inhibitors. *J Med Chem.* 2016;59:1761–1775.
14. Kuo HT, Pan J, Zhang Z, et al. Effects of linker modification on tumor-to-kidney contrast of ^{68}Ga-labeled PSMA-targeted imaging probes. *Mol Pharm.* 2018;15: 3502–3511.
15. Lin KS, Pan J, Amouroux A, et al. In vivo radioimaging of bradykinin receptor B1, a widely overexpressed molecule in human cancer. *Cancer Res.* 2015;75:387–393.
16. Benešová M, Schafer M, Bauder-Wust U, et al. Preclinical evaluation of a tailor-made DOTA-conjugated PSMA inhibitor with optimized linker moiety for imaging and endoradiotherapy of prostate cancer. *J Nucl Med.* 2015;56:914–920.
17. Amouroux G, Pan J, Jenni S, et al. Imaging bradykinin B1 receptor with ^{68}Ga-labeled [des-Arg[10]]Kallidine derivatives: effect of the linker on biodistribution and tumor uptake. *Mol Pharm.* 2015;12:2879–2888.
18. Lin KS, Amouroux G, Pan J, et al. Comparative studies of three ^{68}Ga-labeled [des-Arg[10]]kallidin derivatives for imaging bradykinin B1 receptor expression with PET. *J Nucl Med.* 2015;56:622–627.
19. Zhang Z, Amouroux G, Pan J, et al. Radiolabeled B9958 derivatives for imaging bradykinin B1 receptor expression with positron emission tomography: effect of the radiolabel-chelator complex on biodistribution and tumor uptake. *Mol Pharm.* 2016;13:2823–2832.
20. Stabin MG, Sparks RB, Crowe E. OLINDA/EXM: the second-generation personal computer software for internal dose assessment in nuclear medicine. *J Nucl Med.* 2005;46:1023–1027.
21. Keenan MA, Stabin MG, Segars WP, Fernald MJ. RADAR realistic animal model series for dose assessment. *J Nucl Med.* 2010;51:471–476.
22. Stabin MG, Xu XG, Emmons MA, Segars WP, Shi C, Fernald MJ. RADAR reference adult, pediatric, and pregnant female phantom series for internal and external dosimetry. *J Nucl Med.* 2012;53:1807–1813.
23. Stabin MG, Konijnenberg MW. Re-evaluation of absorbed fractions for photons and electrons in spheres of various sizes. *J Nucl Med.* 2000;41:149–160.
24. Kirschner AS, Ice RD, Beierwaltes WH. Radiation dosimetry of [131]I-19-iodocholesterol: the pitfalls of using tissue concentration data [reply]. *J Nucl Med.* 1975;16:247–249.
25. Wessels BW, Bolch WE, Bouchet LG, et al. Bone marrow dosimetry using blood-based models for radiolabeled antibody therapy: a multiinstitutional comparison. *J Nucl Med.* 2004;45:1725–1733.
26. Kuo HT, Lepage ML, Lin KS, et al. One-step ^{18}F-labeling and preclinical evaluation of prostate-specific membrane antigen trifluoroborate probes for cancer imaging. *J Nucl Med.* 2019;60:1160–1166.
27. Dumelin CE, Trussel S, Buller F, et al. A portable albumin binder from a DNA-encoded chemical library. *Angew Chem Int Ed Engl.* 2008;47:3196–3201.
28. Soeda F, Watabe T, Naka S, et al. Impact of ^{18}F-PSMA-1007 uptake in prostate cancer using direct peptide concentrations: preclinical PET/CT study in mice. *J Nucl Med.* 2019;60:1594–1599.
29. Wurzer A, Pollmann J, Schmidt A, Reich D, Wester H-J, Notni J. Molar activity of Ga-68 labeled PSMA inhibitor conjugates determines PET imaging results. *Mol Pharm.* 2018;15:4296–4302.
30. Chatalic KLS, Heskamp S, Konijnenberg M, et al. Towards personalized treatment of prostate cancer: PSMA I&T, a promising prostate-specific membrane antigen-targeted theranostic agent. *Theranostics.* 2016;6:849–861.
31. Kratochwil C, Giesel FL, Leotta K, et al. PMPA for nephroprotection in PSMA-targeted radionuclide therapy of prostate cancer. *J Nucl Med.* 2015;56:293–298.
32. Borgna F, Deberle LM, Cohrs S, Schibli R, Muller C. Combined application of albumin-binding [^{177}Lu]Lu-PSMA-ALB-56 and fast-cleared PSMA inhibitors: optimization of the pharmacokinetics. *Mol Pharm.* 2020;17:2044–2053.
33. Rousseau E, Lau J, Kuo HT, et al. Monosodium glutamate reduces ^{68}Ga-PSMA-11 uptake in salivary glands and kidneys in a preclinical prostate cancer model. *J Nucl Med.* 2018;59:1865–1868.
34. Harsini S, Saprunoff H, Alden T, Mohammadi B, Wilson D, Benard F. The effects of monosodium glutamate on PSMA radiotracer uptake in men with recurrent prostate cancer: a prospective, randomized, double-blind, placebo-controlled intra-individual imaging study. *J Nucl Med.* May 8, 2020 [Epub ahead of print].
35. Roy J, Warner BM, Basuli F, et al. Comparison of prostate-specific membrane antigen expression levels in human salivary glands to non-human primates and rodents. *Cancer Biother Radiopharm.* 2020;35:284–291.
36. Violet J, Jackson P, Ferdinandus J, et al. Dosimetry of ^{177}Lu-PSMA-617 in metastatic castration-resistant prostate cancer: correlations between pretherapeutic imaging and whole-body tumor dosimetry with treatment outcomes. *J Nucl Med.* 2019;60:517–523.